ISIJ International, Vol. 55 (2015), No. 5, pp. 1048–1057

Bending Formability of Ferritic Stainless Steels for Application to Tubular Exhaust Manifolds

Yang Jin CHUNG,[1)] Frederic BARLAT[2)] and Myoung-Gyu LEE[3)]*

1) POSCO Global R&D Center, Songdo, Yeongsu-gu, Incheon, 545-090 South Korea.
2) Graduate Institute of Ferrous Technology, Pohang University of Science and Technology (POSTECH), Hyoja-dong, Pohang, 790-784 South Korea.
3) Department of Materials Science and Engineering, Korea University, Anam-dong, Seongbuk-gu, Seoul, 136-701 South Korea.

(*Received on November 10, 2014; accepted on January 26, 2015*)

In this study, the bending formability of tubular pipes made of ferritic stainless steels during the rotary bending process was investigated. Three different types of ferritic stainless steel—STS 439, STS 429EM, and STS 441—were selected as the test materials. Finite element (FE) simulations were introduced to predict maximum bending angles, or equivalently the bending formability, for both as-received and annealed tubes. The results from experiments and FE simulations suggest the following main conclusions. First, the pipe materials used in the rotary bending process were subjected to prior work hardening during the tubing process, which resulted in reduced formability. However, proper heat treatment could enhance the bending formability. The optimum annealing conditions were determined from the microstructure analysis and mechanical assessments by uni-axial tensile tests for various heat-treated samples. An annealing temperature/holding time of 900°C/10–60 s resulted in enhanced formability without grain coarsening for the three tested ferritic stainless steels. Second, a FE model predicted maximum bending angles and thinning profiles at the extrados of pipes for both as-received and heat-treated tubes when the boundary conditions and friction coefficients were properly optimized.

KEY WORDS: rotary bending; formability; FEM; annealing.

1. Introduction

Stainless steels have been increasingly applied to automotive exhaust systems for improving fuel efficiency. For example, a tubular exhaust manifold made of stainless steel has become popular owing to its lightweight design. A typical manufacturing process for this type of exhaust manifold is bending, which requires quantitative data for the proper selection of material and its formability.[1,2)] As a component of the exhaust system, the exhaust manifold is the part closest to the engine and is thus exposed to high temperatures. Consequently, this structure is usually manufactured by casting. Recently, a shell-type or tubular exhaust manifold made of steel sheets for lightweight automotive design has drawn significant attention.

The base materials used for a typical exhaust manifold are usually austenitic or ferritic stainless steels, given their high temperature strength, hot corrosion characteristics, and fatigue-proof properties at elevated temperature. Austenitic stainless steels are usually superior to ferritic stainless steels in terms of their high temperature strength and thermal fatigue properties, although they are more expensive. In contrast, ferritic stainless steels have inferior strength at high temperatures but good fatigue properties owing to their smaller thermal expansion coefficients.[3–5)] In addition, they are also cost-effective because of the absence of Ni as an expensive additive.

The formability of ferritic stainless steel sheets is inferior to that of austenitic stainless steel sheets. This hurdle must also be overcome before applying forming technologies to manufacture lightweight exhaust manifolds. For example, although a tube bending step is required as a pre-forming process in hydroforming technology, the low formability of ferritic stainless steels may lead to premature failure during the bending process as the final target components become complicated.[6)]

Exhaust manifolds can be classified into two general types depending on the manufacturing process: the stamping type, which is formed by pressing; and the tubular type, which is made of pipes. The stamping-type exhaust manifold is obtained by welding together upper and lower parts of the shell type. However, the durability of this type of exhaust manifold is poor in the welding region, where considerable thermal stress may develop by thermal cycling. This is because the part formed by stamping inevitably includes a long welding line and an irregular bead shape. On the other hand, the tubular exhaust manifold is processed from a runner pipe, which has superior welding quality because it is made of automatically welded skelp. Moreover, the smaller area of the weld line in this type of exhaust manifold results in better thermal fatigue properties. Because manufacturing

* Corresponding author: E-mail: myounglee@korea.ac.kr
DOI: http://dx.doi.org/10.2355/isijinternational.55.1048

the tubular exhaust manifold involves rotary pipe bending,[7] appropriate formability must be guaranteed to avoid wrinkling or fracture during the bending process. Adequate control of springback, an elastically driven change in shape following bending, is also required for the tubular manifold to be fitted with other parts[8–10]. In particular, recent automotive designs require runner parts with more complex shapes, for which a smaller bending radius is beneficial to secure higher degrees of freedom in terms of the design of the engine exhaust system.

The aim of the present study is to develop a numerical tool to predict the formability of ferritic stainless tubular parts in the rotary bending process. First, proper heat treatment conditions are determined by experiment for different types of stainless steels. Subsequently, finite element (FE) analysis is used to predict the maximum bending angle tolerated during the bending process without resulting in failure.

2. Materials and Heat Treatment

Typical materials used for automotive exhaust manifolds are ferritic stainless steels (FSS) such as STS 439, STS 429EM, STS 441, and STS 444. Among these, STS 439 has been widely used for exhaust system components owing to its highly corrosion-resistant properties attained with the addition of 18% Cr. STS 429EM has less Cr; however, increasing the Si content improves its resistance to high temperature oxidation. STS 441 is similar in chemical composition to STS 439, but is designed to have superior high temperature strength with the addition of Nb. STS 444 contains 19% Cr and 2% Mo, which leads to enhanced strength and corrosion resistance at high temperatures.

In this study, STS 439, STS 429EM, and STS 441 were selected as the test materials for the automotive exhaust manifold. All three materials were 2 mm thick and formed into pipes with an outer radius of 34 mm by electric resistance weld (ERW) seam welding. The prior deformation during tubing decreases the ductility of the pipes relative to that of the original sheet materials. Therefore, a heat treatment process is frequently employed before bending of the pipe to improve its formability. One aim of the present study is to investigate the effect of heat treatment on the bending formability of pipes made of stainless steel. Additionally, microscopic and mechanical analyses are conducted to identify the optimum heat treatment conditions. **Figure 1** shows an annealing heat treatment condition adopted in this study, with a holding time of 10 s. First, a 450-mm pipe was inserted into a box furnace and kept there for 360 s before it reached a target temperature. Then, it was held isothermally for a specified time, removed from the furnace, and finally cooled by air. Two holding times, 10 s and 60 s, were considered. The grain size was measured by the ASTM E112-96 standard method. The samples were taken from base material located 180° away from the weld line to exclude welding effects. The grain size was optically measured in the transverse direction (TD). The grain size for each condition is listed in **Table 1** in terms of the ASTM number.

Figure 2 shows the microstructures of the three stainless steels before and after heat treatment. Figure 2(a) shows that grain coarsening was observed for STS 439 when it was annealed at 950°C. For both holding times, the grain

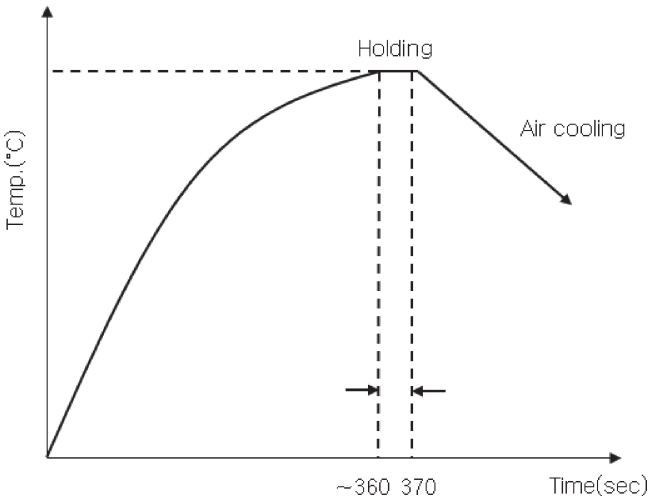

Fig. 1. Annealing conditions.

Table 1. Grain size after annealing.

Temperature (°C)	Holding time (s)	Grain size (ASTM number)		
		439	429EM	441
Before annealing	No data	5.8	5.1	5.1
850	10	5.7	4.8	5.1
	60	5.8	4.8	5.6
900	10	5.7	4.8	5.2
	60	5.3	4.8	5.4
950	10	5.3	5.0	5.1
	60	4.7	5.1	5.4

sizes markedly increased. However, the grain size remained unchanged for all other annealing conditions. For STS 429EM and STS 441, grain coarsening was not observed in any of the annealing conditions considered in this study (Figs. 2(b) and 2(c)).

To assess mechanical properties, tensile samples were cut from pipes by using electrical discharge machining. The dimensions of the samples were in accord with JIS 13B. Tensile tests were conducted in an MTS universal testing machine. The cross-head speed was 20 mm/min and a 50-mm extensometer was used to measure the strain. The measured true stress-strain curves for the three materials are shown in **Fig. 3**. As expected, when the samples were taken from unannealed tubes, the stress-strain curves showed narrow regions of uniform elongation and work softening.

The figure also shows that the yield stresses decreased, although uniform as well as total elongation increased for all three materials after heat treatment. In addition, the tensile strength decreased as the temperature and duration of annealing increased, and showed greater sensitivity to these two factors than did elongation. On the basis of the grain size and tensile properties after heat treatment, an optimum annealing condition of 900°C/10–60 s (annealing temperature/isothermal holding time) was chosen for further analysis.

Hardness was also measured before and after heat treatment to check if the samples were properly annealed. **Table 2** lists the change of Vickers hardness for the three materials

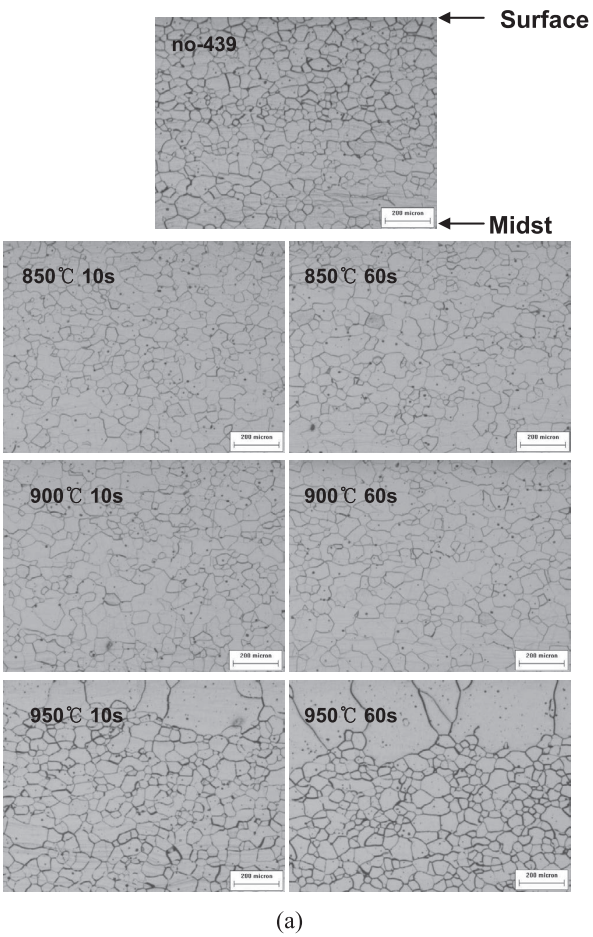

(a)

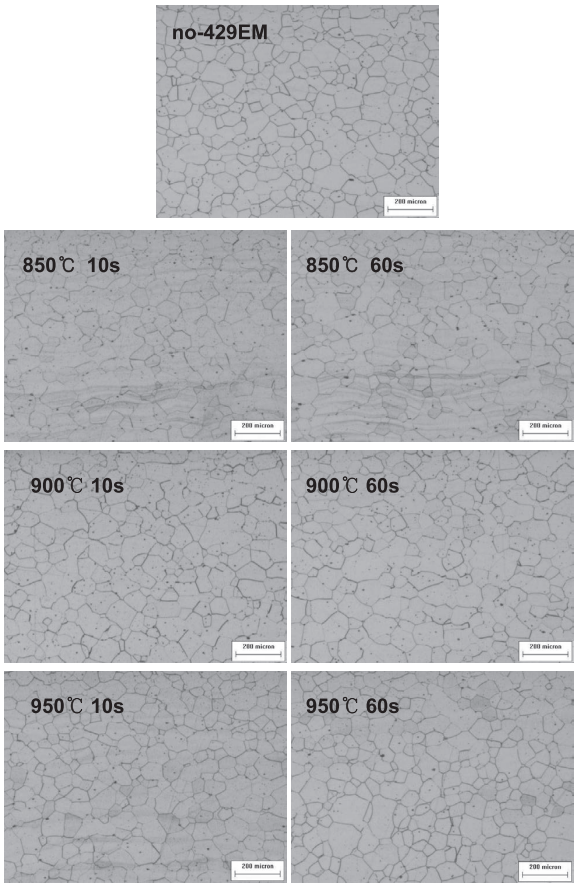

(b)

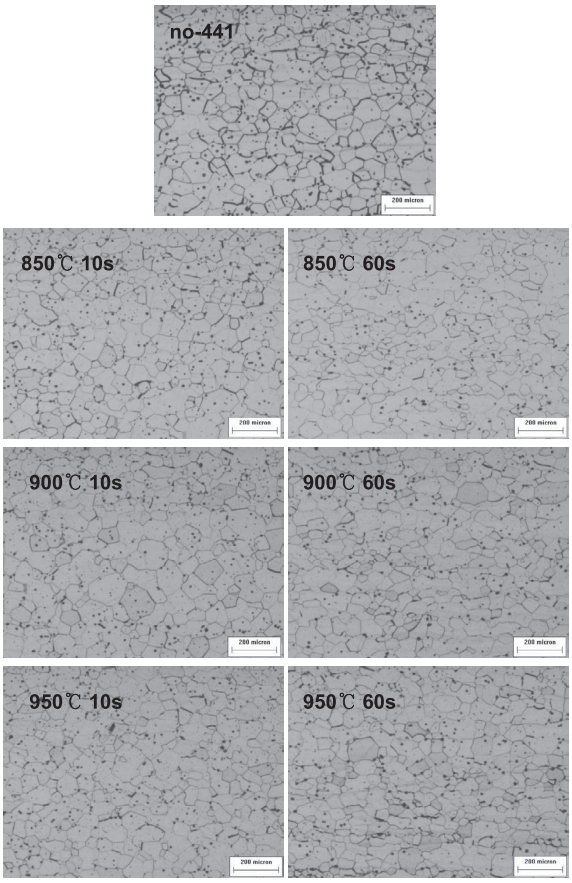

(c)

Fig. 2. Microstructures of pipes before and after heat treatment: (a) STS 439, (b) STS 429EM, and (c) STS 441.

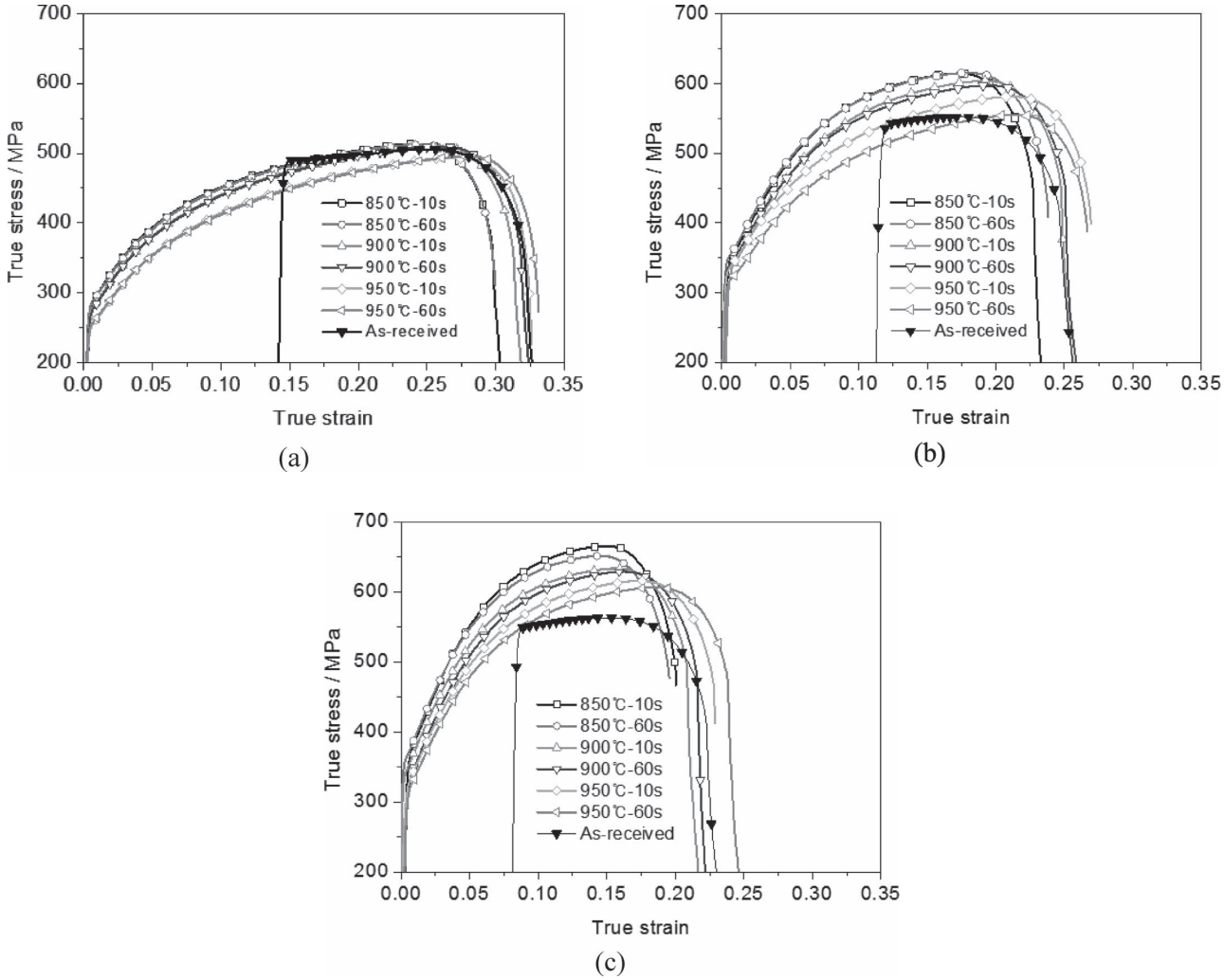

Fig. 3. True stress-strain curves before and after heat treatment: (a) STS 439, (b) STS 429EM, and (c) STS 441.

Table 2. Measured Vickers hardness before and after annealing (unit: Hv).

Material	Annealing condition	Weld zone	Distance from weld zone						
			1 mm	2 mm	3 mm	4 mm	5 mm	6 mm	avg.
439	As-received	191.4	177.7	173.1	175.8	179.1	175.4	173.6	175.8
429EM	As-received	201.2	198.5	202.9	208.9	208.0	195.6	196.2	201.7
441	As-received	197.0	196.2	201.2	195.0	205.3	190.7	193.8	197.0
439	900°C 10 s	147.1	140.4	138.8	134.8	136.2	135.3	136.4	137.0
429EM	900°C 10 s	173.9	166.0	165.9	163.2	164.7	166.2	163.9	165.0
441	900°C 10 s	172.9	169.9	165.0	162.0	165.4	164.2	163.0	164.9

before and after heat treatment. The heat treatment condition was 900°C/10 s on the basis of the previous study on the microstructure and tensile properties. The hardness at the welding zone was also measured to check the variation in hardness near the heat affected zone (HAZ). The hardness values at 6 different spots from the welding zone were averaged. Table 2 shows that the hardness of the welding zone and other spots considerably decreased after heat treatment, confirming that the samples were well annealed. **Figure 4** also shows comparisons of the Vickers hardness for the three materials before and after annealing.

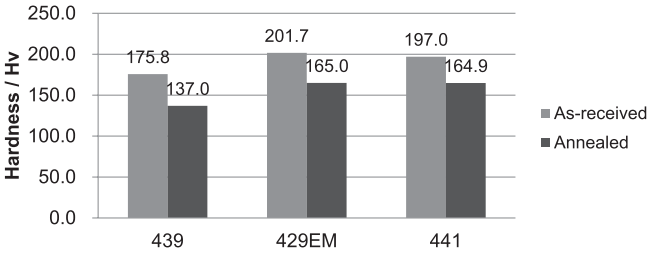

Fig. 4. Comparison of Vickers hardness between as-received and annealed tubes.

The change in the dimensions of the pipe was also investigated to determine the clearance between the tube and die tool. The dimensions of the radius (inner and outer) and thickness are shown in **Tables 3** and **4**, respectively, before

Table 3. Inner/outer radii of tubular pipes before and after heat treatment.

Condition	Outer, Inner	Averaged radius (mm)		
		439	429EM	441
As-received	OD	34.12	34.15	34.16
	ID	29.98	30.20	30.07
Annealed	OD	34.15	34.15	34.13
	ID	30.01	30.23	30.05

Table 4. Thickness of tubular pipe before and after heat treatment.

Condition	Averaged thickness (mm)		
	439	429EM	441
As-received	2.087	1.974	2.050
Annealed	2.090	1.979	2.050

and after annealing. The values of the radius and thickness in the tables are averaged across 5 and 7 repeated measurements, respectively. Statistical analyses revealed no significant change in the dimensions of the pipe and thickness after heat treatment. Therefore, the same tool clearance was used as designed for the as-received pipes.

3. Bending Experiment

Figure 5 shows the equipment for rotary pipe bending used in the current study. The rotary pipe bending tester consists of a bend die, clamp die, pressure die, wiper die, and mandrel. A brief summary on the role of each part is given below. The bend die determines the radius of the bend in the tube, and supports the front part of the pipe. The clamp die fixes the bend die and pipe. The pressure die applies boosting force in the tangential direction of the bending part. The wiper die is connected to the bend die to prevent wrinkles on the tube intrados. Finally, the mandrel plays a role in preventing the collapse of the tube extrados and maintaining the roundness of the tube.

Before testing, a pipe is inserted in the mandrel and fixed by a chuck in the carriage booster. Preparations for the bending test are then completed when the pressure and clamp dies are positioned. During the bending test, the bend and clamp dies rotate simultaneously, and additional boosting force is applied by the booster and pressure dies as the bending process proceeds. Preliminary tests were carried out to determine the optimum process profile. **Figure 6** shows the dimensions of the rotary bending pipe tools. The dimensions are determined for a pipe with an outer radius (OD) of 34 mm. The wall factor (OD/thickness) is 17, and the "DofBend" (or CLR/OD, where CLR is the centerline radius) is 1.2. The DofBend is also called the "bend radius." In the appendix, the generally recommended number of mandrel balls is listed in terms of the wall factor and the DofBend in the rotary pipe bending process. Although the collapse of the pipe extrados generally becomes severe as the DofBend decreases, the cross-sectional shape changes for the proper number of mandrel balls. On the basis of data

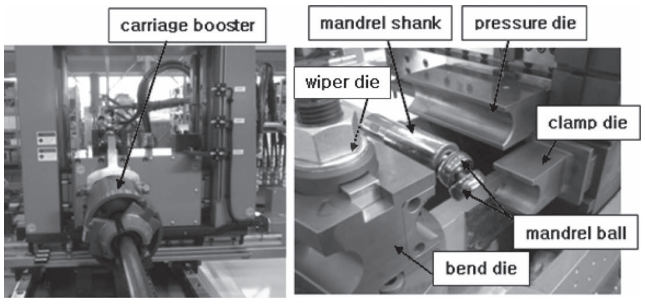

Fig. 5. Tool set for rotary pipe bending machine.

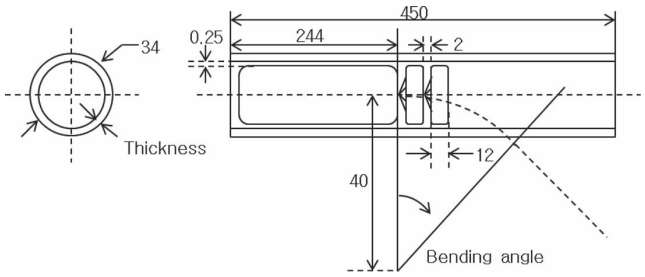

Fig. 6. Dimensions of rotary pipe bending tool and pipe (unit: mm).

in the appendix, the number of mandrel balls is determined as 2. In particular, the horizontal position of the center of the first mandrel ball is located at the center of rotation by retreating mandrel assemblies, which is equivalent to 1.5 mandrel balls. A boosting force of 0 to 20 kN was applied in the current bending test and the former FE-200M lubricant from Yushiro Chemical Industry Co., Ltd. was applied to the inside of the pipe.

In **Fig. 7**, the measured thicknesses after bending for as-received and annealed pipes are shown for the three materials. A micro-meter was used to measure the thickness of the pipe after bending at the elongated region where the fracture is usually observed. The same location starting from a point at extrados, which is shown as $x=0$ in Fig. 7(e), was used to measure the thinning. When necking of the pipe occurred without showing explicit fracture, the evaluation was also complemented by observations with the naked eye. To evaluate tube bending formability, the carriage boosting force and bending angle were identified as the most important parameters, and the thickness reduction ratio was chosen as the parameter to determine the fracture criterion. Figure 7 shows thickness reduction ratios in terms of the carriage boosting force and bending angle. For all cases, thickness reduction (*i.e.*, thinning) increased as the bending angle increased. The bending angle at fracture also increased markedly when the material was heat treated. Note that because of missing data for STS 441 (Fig. 7(e)), the formability is analyzed in detail only for STS 439 and STS 429EM in the following sections. From the experimental results, the fracture criteria (*i.e.*, thickness reduction ratios) of the three materials for both as-received and heat-treated conditions were as follows: 35% for STS 439, 32.5% for STS 429EM, and 32.5% for STS 441. When thickness reductions exceeded these values, the extrados of the pipes were assumed to have undergone either localized necking or fracture.

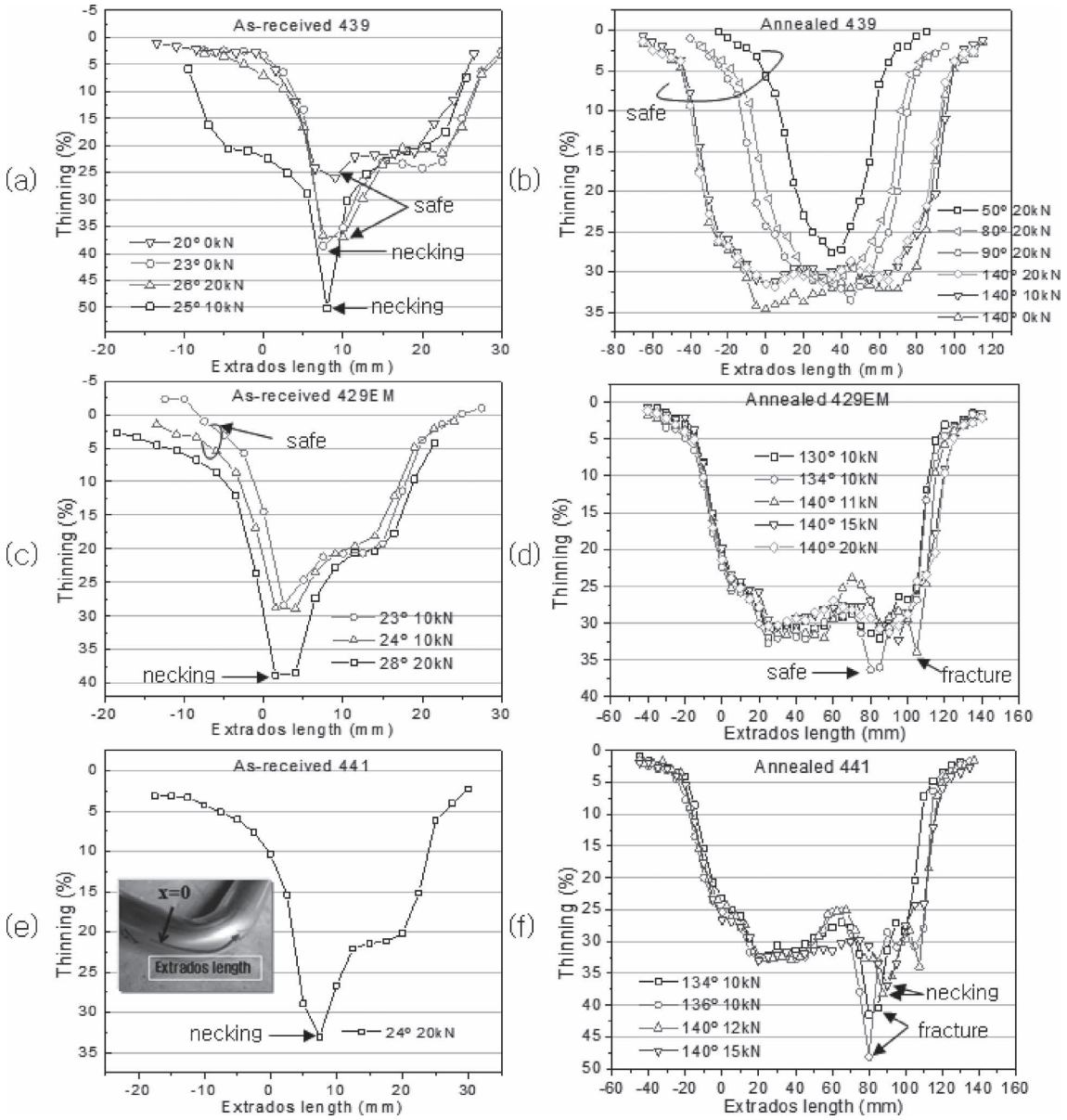

Fig. 7. Thinning distribution along the extrados of pipes: (a) as-received STS 439, (b) annealed STS 439, (c) as-received STS 429EM, (d) annealed STS 429EM, (e) as-received STS 441, and (f) annealed STS 441. Localized necking and fracture were indicated in the selected bending conditions.

4. Result and Discussion

4.1. Finite Element Analysis

Deformation in the pipe bending process was analyzed by FE simulations. Tools in the pipe bending process were generated by using the commercial FE software Pam-Stamp®, in which built-in tool models are provided. The size of the mandrels and the interval between them were modified to the same dimensions as in the experiments. The pipe bending process was simulated by the commercial FE software LS-Dyna3D™. A 4-node shell element was used to model the pipe, and a smaller mesh of 1 mm was used in the potential fracture region to capture plastic deformation behavior more accurately during deformation. The whole FE model, including the pipe, mandrel, and tools, is shown in **Fig. 8**. Isotropic elastic-plastic constitutive equations for the three materials were used. Although anisotropic models could have been used for more accurate deformation analysis, isotropic properties were assumed for simplicity. The von

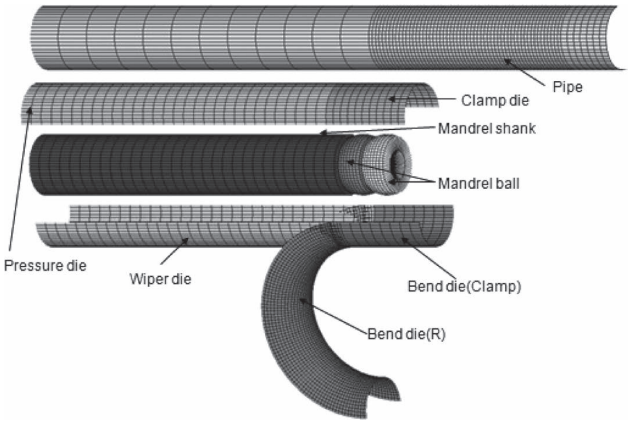

Fig. 8. Finite element model for rotary pipe bending simulation.

Mises isotropic yield function was applied with the Swift hardening model. The hardening curves fitted to the Swift equation are shown in **Fig. 9** for both as-received and heat-

treated materials.

The carriage boosting force was simulated by constraining the nodes at the pipe end. The boosting force was kept constant during bending. Force in the pressure die was not applied because only frictional force is present during bending. This boundary condition is reasonable because the main role of the pressure die is to support the wiper die and pipe. A critical parameter in FE modeling is the friction between the pipe and tools. In this study, the friction coefficients between the tools and pipe were determined by comparing the simulated and measured values of sheet thinning. In **Fig. 10**, the measured thickness reductions along the pipe extrados are compared with the simulated thickness variations when the best-fitting friction coefficients were used. The six best-fitting friction coefficients are listed in **Table 5**.

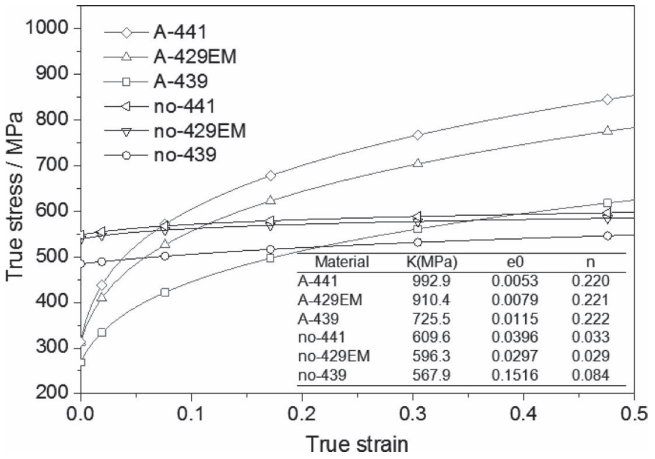

Fig. 9. Stress-strain curves and their material parameters for Swift hardening law (no-441 denotes the stress-strain curve of unannealed 441 steel).

A significant higher value of friction coefficient was applied to the interfaces between tube and clamp, and between tube and bend dies to simulate a non-slip condition in the real process. In Table 5, the friction coefficients for the two contact surfaces are assumed as 10, which efficiently prevents the slipping during the simulation. In fact, a preliminary study showed no slipping between the tools and pipe when the friction coefficient was larger than 2. In the experiment, protrusions were added to the (clamp die) tool surface to prevent slipping between the clamping tool and pipe. The friction coefficient in the bend die was decomposed into two components. In the early stage of the bending process, the pipe contacted the straight region of the bend die (denoted as "Bend die (Clamp)" in Table 5), where a very high friction coefficient was assigned to clamp the pipe. However, when the pipe came into contact with the curved region of the bend die (denoted as bend die (R)), a friction coefficient of 0.1 was assigned. This value has been used frequently in simulations of sheet metal forming. The

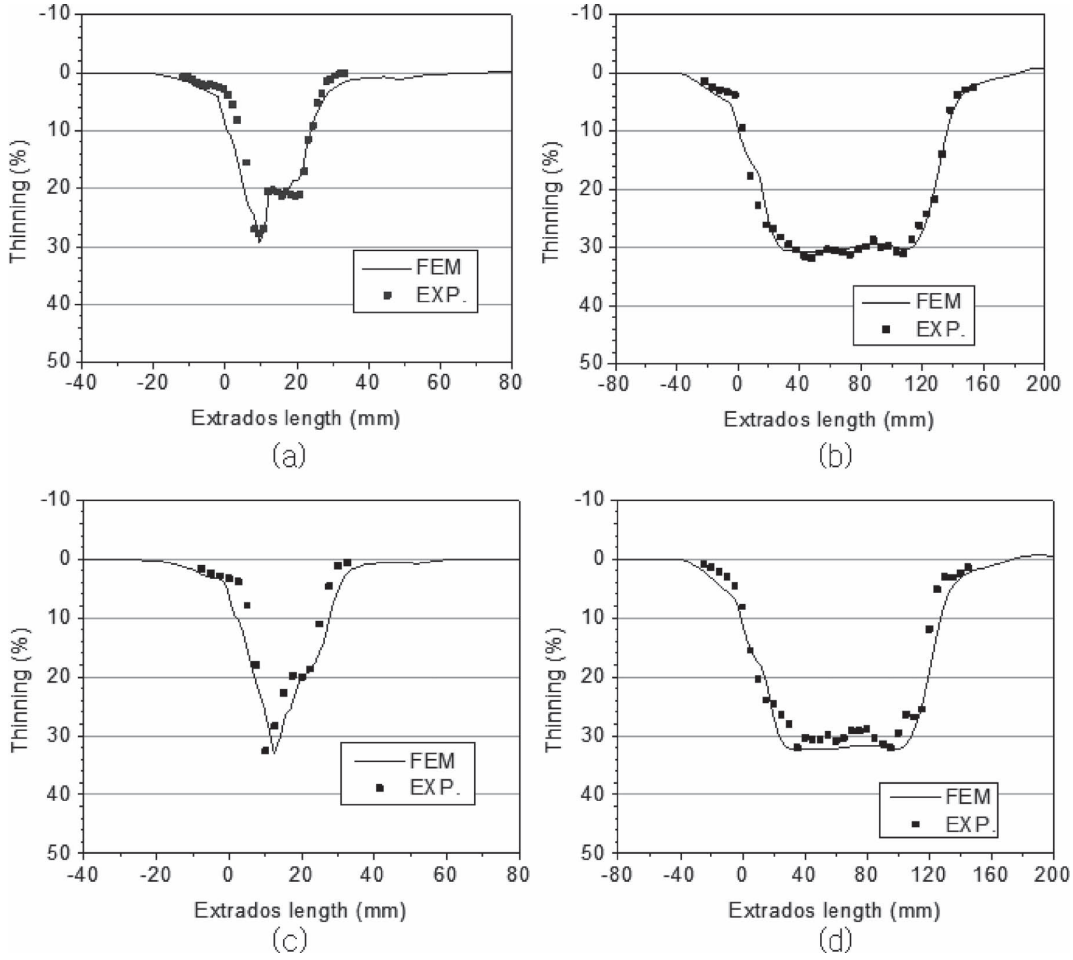

Fig. 10. Simulated and measured thinning profiles after pipe bending: (a) as-received STS 439/20°/0 kN, (b) annealed STS 439/140°/20 kN, (c) as-received STS 429EM/23°/0 kN, and (d) annealed STS 429EM/130°/10 kN.

Table 5. Best fitting friction coefficients for contact surfaces of bending tool.

Contact1	Contact2	Friction coefficient	Remark
Tube	Mandrel shank	0.03	Clearance between tube and mandrel was altered in annealed case,
Tube	Mandrel ball	0.03	
Tube	Pressure/Wiper die	0.85	
Tube	Clamp	10	
Tube	Bend die (Clamp)	10	
Tube	Bend die (R)	0.1	

Table 6. Comparison between measured and FE predicted maximum bending angles.

	Steels	Boosting force	Bending angle (EXP.)	Bending angle (FEM)
As-received pipes	439	0 kN	23°	22.1°
		2 kN	27°	27°
	429EM	0 kN	23°	20.1°
		2 kN	26°	27.2°
Annealed pipes	439	0 kN	>140°	>140°
		2 kN	>140°	>140°
	429EM	0 kN	49°	47.6°
		2 kN	>140°	146.5°

friction coefficient between the pipe and mandrel decreased than 0.1, and the friction coefficient between the pipe and mandrel ball was also assumed to be quite low value owing to sufficient lubrication in the real process. The other two contact conditions—between the pipe and pressure die and between the pipe and wiper die—were obtained from iterative inverse FE analysis by comparing the experimental and simulated thinning profiles of the tube at the extrados. The best-fitting friction conditions are listed in Table 5. Figure 10 shows that the thinning profiles calculated by applying the determined friction coefficients were in good agreement with the experimental results for the three materials at different bending angles and boosting forces. The friction coefficients in **Table 6** will be used for further analyses to evaluate the critical bending angles at localized necking or fracture sites.

4.2. Analysis of Bending Formability

To evaluate the maximum bending angle before localized necking or fracture, simulations were performed for the three materials. The thickness reductions of elements in the area of interest (AOI) were traced as the bending angle increased. When thinning in a particular element exceeded the experimentally evaluated values, the bending angle was regarded as the maximum angle associated with the forming limits of the pipe. When the thicknesses of all finite elements in the AOI were plotted as a function of bending angle, the element representing maximum thinning changed as bending proceeded. **Figure 11**(a) shows the thickness changes of representative elements (marked A–G) in the AOI during the bending process of as-received STS 439 with a boosting force of 20 kN. At the early bending stage, the element representing maximum thinning was located near the mandrel ball (E, F). However, as bending proceeded, the element with maximum thinning passed through the mandrel ball, which explains why the position of maximized thinning changed during the bending process. Therefore, predicting the maximum bending angle (or pipe formability) precisely requires that the thinning profiles of all elements in the AOI be traced. Figure 11(b) shows the thickness distribution of the tube after a 25° bend. In this figure, the element at location D showed the maximum thickness reduction and thinning decreased as the position increased in distance from element D. Thinning of element D occurred abruptly after a 25° bend, although other elements did not show such abrupt changes. This is because the localization is concentrated on element D. Consequently, a detailed analysis resulted in a bending formability of 27° when considering the limit thinning strain of 35% obtained in the previous analysis. The maximum bending angles predicted by the above procedure are listed in Table 6 along with the experimental values. Both as-received and heat-treated pipes made of STS 349 and STS 429 for two prescribed boosting forces were considered. As the table shows, the maximum bending angles

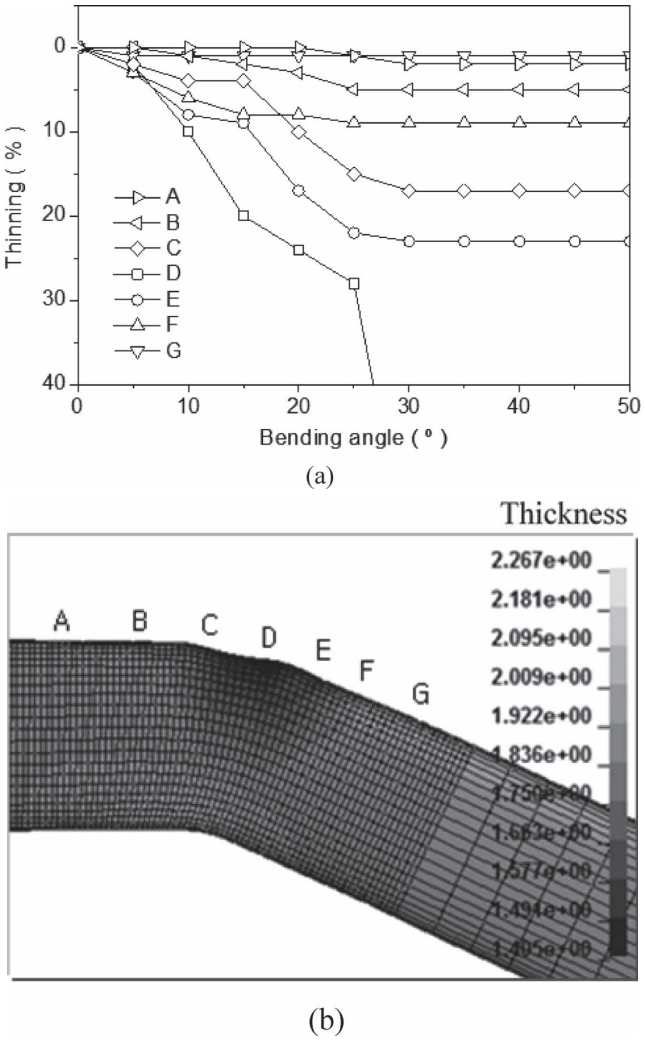

Fig. 11. Thinning history as a function of bending angle calculated by finite element simulations for as-received STS 439 at a boosting force of 20 kN: (a) thinning profiles of several elements at the extrados of pipe as the bending angle increases, and (b) thickness distribution at a bending angle of 25°.

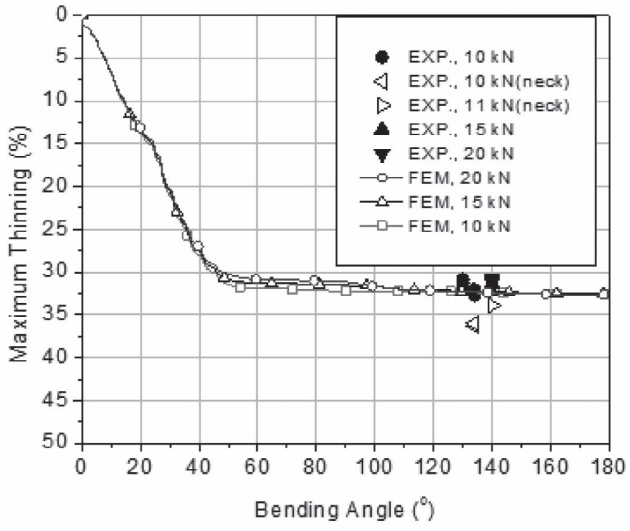

(a)

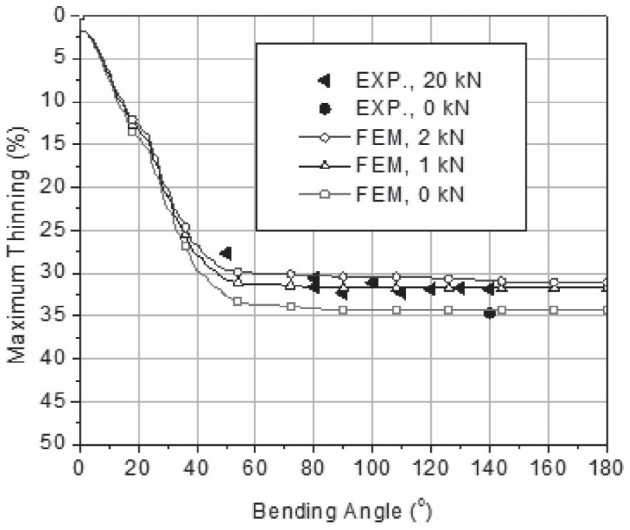

(b)

Fig. 12. Comparison between predicted and measured maximum thinning profiles during pipe bending: (a) annealed STS 429EM, and (b) annealed STS 439.

predicted by FE simulations were in very good agreement with the experimentally measured values. In particular, the maximum bending angles for the as-received pipe (without heat treatment) were well predicted with considerable accuracy. In the experiments, the maximum attainable bending angle was 140°; bending can continue to this limit, particularly for heat-treated materials. In this case, the bend in the pipe is assumed to be devoid of fractures. The table shows that the experimental and simulated maximum bending angles were also in good agreement for the heat-treated pipes as well. In **Fig. 12**, the calculated maximum thinning as a function of bending angle is presented together with the experimental data. For heat-treated STS 429EM, the calculated thinning agrees closely with the experimentally measured thinning at a 130° bend. Similarly, Fig. 12(b) shows that the maximum thinning history with respect to the bending angle agrees well with the measured result.

5. Conclusion

In this study, a numerical tool was proposed to predict the bending formability of pipes made of ferritic stainless steel during the rotary bending process. Three different types of ferritic stainless steel (STS 439, STS 429EM, and STS 441) were selected as test materials. The following conclusions were drawn from the experiments and FE simulations.

(1) The pipe materials used in rotary bending are subjected to work hardening during the tubing process. This prior working hardening reduces the formability of the pipe during bending. Therefore, proper heat treatment is required to enhance the bending formability before the rotary bending process. In this study, optimum annealing conditions were determined from the microstructure analysis and mechanical assessment by uni-axial tensile tests. An annealing temperature/holding time of 900°C/10–−60 s resulted in enhanced ductility without grain coarsening for the three tested ferritic stainless steels.

(2) Heat treatment markedly improved bending formability, as determined by analyses of the microstructure and mechanical properties.

(3) A FE model was constructed for the rotary pipe bending process. For accurate FE modeling, the boundary conditions and friction coefficients between the pipe and tools were optimized by comparing the measured and calculated thinning profiles at the extrados of pipes made of STS 439 and STS 429EM. The best-fitting friction coefficients are listed in Table 6.

(4) On the basis of the measured maximum thinning criteria for the three tested materials, the proposed FE model accurately predicted the maximum bending angle without failure in the rotary bending process. The predicted thinning profiles as a function of the bending angle were in good agreement for both as-received and heat-treated pipes.

Acknowledgement

The authors appreciate supports by the National Research Foundation of Korea (NRF) Grant funded by the Korea government (MSIP) (NRF-2014R1A2A1A11052889) and ERC program (NRF-2012R1A5A1051500).

REFERENCES

1) J. Miller, S. Kyriakides and A. Bastard: *Int. J. Mech. Sci.*, **43** (2001), 1183.
2) J. Miller and S. Kyriakides: *Int. J. Mech. Sci.*, **45** (2003), 115.
3) F. Stachowicz, T. Trzepieciński and T. Pieja: *Arch. Civ. Mech. Eng.*, **10** (2011), 85.
4) H. Takuda, K. Mori, T. Masachika, E. Yamazaki and Y. Watanabe: *J. Mater. Process Technol.*, **143** (2003), 242.
5) I. Lonardelli, P. Bosetti, S. Bruschi and A. Molinari: *Key Eng. Mater.*, **473** (2011), 869.
6) J. Bong, F. Barlat, D. Ahn, H. Kim and M. Lee: *Int. J. Mech. Sci.*, **75** (2013), 94.
7) J. Liu, H. Yang, M. Zhang and Z. Jiang: *Compt. Mater. Sci.*, **60** (2012), 113.
8) H. Laurent, R. Greze, P. Manach and S. Thuiller: *Int. J. Mech. Sci.*, **51** (2009), 233.
9) C. Pham, S. Thuillier and P. Manach: *J. Mater. Process Technol.*, **214** (2014), 844.
10) J. Liao, X. Xue, M. Lee, F. Barlat and J. Gracio: *Int. J. Mech. Sci.*, **89** (2014), 311.

Appendix. Reference chart for the tool selection in the rotary pipe bending.

Wall Factor	D of Bend							
	1	*1.25*	*1.5*	*2*	*2.5*	*3*	*4*	*5*
8–12	1 ball	1 ball	1 ball	plug	plug	plug	–	–
	Wiper	Wiper	–	–	–	–	–	–
13–17	2 ball	1 ball	1 ball	1 ball	plug	plug	–	–
	wiper	Wiper	–	–	–	–	–	–
18–22	3 ball	2 ball	2 ball	1 ball	1 ball	1 ball	plug	–
	wiper	Wiper	wiper	–	–	–	–	–
23–27	3 ball	2 ball	2 ball	2 ball	2 ball	1 ball	1 ball	Plug
	wiper	Wiper	wiper	wiper	wiper	–	–	–
28–32	3 ball	3 ball	3 ball	2 ball	2 ball	2 ball	1 ball	Plug
	wiper	Wiper	wiper	wiper	wiper	wiper	–	–
33–37	3 ball	3 ball	3 ball	2 ball	2 ball	2 ball	2 ball	1 ball
	wiper	Wiper	Wiper	wiper	wiper	wiper	wiper	–
38–44	4 ball	3 ball	3 ball	3 ball	3 ball	3 ball	2 ball	2 ball
	wiper	Wiper	Wiper	wiper	wiper	wiper	wiper	–